

2020

Structural characterization of TssL from *Acinetobacter baumannii*: A key component of the type VI secretion system

Federico M Ruiz

Centro de Investigaciones Biológicas Margarita Salas

Juvenal Lopez

Washington University School of Medicine in St. Louis

C Gastón Ferrara

National University Arturo Jauretche

Elena Santillana

Centro de Investigaciones Biológicas Margarita Salas

Yanis R Espinosa

Universidad Industrial de Santander

See next page for additional authors

Follow this and additional works at: https://digitalcommons.wustl.edu/open_access_pubs

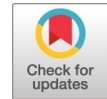
Recommended Citation

Ruiz, Federico M; Lopez, Juvenal; Ferrara, C Gastón; Santillana, Elena; Espinosa, Yanis R; Feldman, Mario F; and Romero, Antonio, "Structural characterization of TssL from *Acinetobacter baumannii*: A key component of the type VI secretion system." *Journal of Bacteriology*,. . (2020).
https://digitalcommons.wustl.edu/open_access_pubs/9318

This Open Access Publication is brought to you for free and open access by Digital Commons@Becker. It has been accepted for inclusion in Open Access Publications by an authorized administrator of Digital Commons@Becker. For more information, please contact engeszer@wustl.edu.

Authors

Federico M Ruiz, Juvenal Lopez, C Gastón Ferrara, Elena Santillana, Yanis R Espinosa, Mario F Feldman, and Antonio Romero



Structural Characterization of TssL from *Acinetobacter baumannii*: a Key Component of the Type VI Secretion System

Federico M. Ruiz,^a Juvenal Lopez,^b C. Gastón Ferrara,^{c,d} Elena Santillana,^a Yanis R. Espinosa,^e Mario F. Feldman,^b Antonio Romero^a

^aChemical and Physical Biology, Centro de Investigaciones Biológicas Margarita Salas, Madrid, Spain

^bDepartment of Molecular Microbiology, Washington University School of Medicine in St. Louis, St. Louis, Missouri, USA

^cSchool of Engineering and Agronomy, National University Arturo Jauretche, Florencio Varela, Argentina

^dInstitute of Physics of Liquids and Biological Systems (IFLYSIB), CONICET-National University of La Plata, La Plata, Argentina

^eGrupo de Bioquímica Teórica, Universidad Industrial de Santander, Bucaramanga, Colombia

ABSTRACT The type VI secretion system (T6SS) is a complex molecular nanomachine used by Gram-negative bacteria to deliver diverse effectors into adjacent cells. A membrane complex (MC) anchors this transport system to the bacterial cell wall. One of the proteins forming the MC is TssL, a cytoplasmic protein bound to the inner membrane through a single transmembrane helix. Here, we report the structure of the cytoplasmic N-terminal region of TssL from *Acinetobacter baumannii*, a bacterium encoding in a single locus a secretion system that is a special case among other T6SSs. The protein structure, consisting of two antiparallel alpha-helical bundles connected by a short loop, reveals several interesting particularities compared with homologous proteins from other organisms. In addition, we demonstrate the structural significance of residues Asp98 and Glu99, which are strongly conserved among T6SS-encoding Gram-negative bacteria. Mutations in these two residues strongly impact protein dynamics, expression, and functionality. Our results improve our understanding of the T6SS of *A. baumannii*, which remains largely understudied compared with that of other pathogens.

IMPORTANCE Several *Acinetobacter* species carry one functional type VI secretion system (T6SS). The T6SS is encoded in a single locus containing 16 conserved genes, most of which code for proteins essential to T6SS activity. One of these key components is TssL, a cytoplasmic protein bound to the inner membrane. Despite its importance and its particular characteristics, the structure of T6SS in *A. baumannii* remains understudied. Here, we present structural, *in silico*, and *in vivo* studies of TssL, highlighting the importance of two well-conserved residues and improving our understanding of this secretion system in this bacterium.

KEYWORDS *Acinetobacter*, secretion systems, structural biology

Bacteria use a wide variety of membrane transport systems to deliver toxins to the extracellular milieu or directly into target cells. These molecular nanomachines, and the associated secreted proteins, play an important role in bacterium-host interactions and in interbacterial competition. The type VI secretion system (T6SS) is widespread among Gram-negative bacteria and targets both eukaryotic and prokaryotic cells in a contact-dependent manner. The structure, composition, and dynamics of this protein complex have been best characterized for *Escherichia coli* (1). In this model organism, 13 conserved proteins (TssA to -M) build the T6SS machine, which structurally resembles a bacteriophage tail anchored to the bacterial membrane (2). When the T6SS is activated, contraction of a sheathlike structure (TssBC) drives an effector-loaded tube complex, made of Hcp (TssD) and VgrG (TssI), out of the bacterial cell and into adjacent

Citation Ruiz FM, Lopez J, Ferrara CG, Santillana E, Espinosa YR, Feldman MF, Romero A. 2020. Structural characterization of TssL from *Acinetobacter baumannii*: a key component of the type VI secretion system. *J Bacteriol* 202:e00210-20. <https://doi.org/10.1128/JB.00210-20>.

Editor Ann M. Stock, Rutgers University-Robert Wood Johnson Medical School

Copyright © 2020 American Society for Microbiology. All Rights Reserved.

Address correspondence to Federico M. Ruiz, frui@cib.csic.es, or Antonio Romero, romero@cib.csic.es.

Received 12 April 2020

Accepted 12 June 2020

Accepted manuscript posted online 22 June 2020

Published 10 August 2020

target cells. This contractile structure is assembled onto a baseplate complex (BC), which is, in turn, anchored to the cell envelope by a membrane complex (MC). Proteins TssE, TssF, TssG, TssK, and VgrG constitute the BC, while TssJ, TssL, and TssM form the MC (3, 4). These last three proteins are recruited in a specific order starting with the outer membrane lipoprotein TssJ, then the alpha-helical envelope-spanning TssM, and finally TssL (5).

TssL is essential for Hcp secretion, a hallmark of a functional T6SS (6). Structural characterization of TssL from *E. coli* revealed an all-alpha-helical secondary structure divided into N- and C-terminal bundles linked by a flexible loop (6), an arrangement also observed in *Francisella novicida* and *Vibrio cholerae* (7, 8). TssL is anchored to the bacterial inner membrane through a single C-terminal transmembrane helix (TMH) (9). This TMH mediates the dimerization of TssL, a process that is essential for proper T6SS assembly (10). TssL dimerization is proposed to occur via a zipper-like mechanism in which interactions between the TMHs of TssL monomers increase the local concentration to favor the subsequent association between their cytoplasmic domains (6). The cytoplasmic domain of TssL mediates essential interactions between TssL and components of the MC and BC. For instance, TssL interacts with the cytoplasmic domain of TssM through a cleft lying in the highly conserved interface between both TssL helix bundles (3, 7). Additionally, TssL interacts with BC components TssK and TssE through flexible loops connecting helices in the N- and C-terminal bundles, respectively. Thus, TssL plays a critical role in T6SS function by linking the MC to the BC via low-affinity interactions, which have been proposed to be critical to the conformational transitions that are required for the dynamics of the T6SS machine (3). However, it remains unknown whether the findings in *E. coli* are widely applicable to the T6SSs of other Gram-negative bacteria.

Acinetobacter baumannii is a Gram-negative bacillus that has recently emerged as an opportunistic human pathogen, having an alarmingly high ability to develop multidrug resistance (11–14). Described for the first time in a lipopolysaccharide (LPS)-deficient strain (15), a functional T6SS is broadly distributed among *Acinetobacter* species (16–18). In these bacteria, the T6SS is encoded in a single locus containing 16 conserved genes, most of which code for proteins essential to T6SS activity (16, 19). Interestingly, they lack a clear homolog of TssJ, making their membrane complex a special case among other T6SSs (16). Moreover, a recent study showed that unlike in *E. coli*, the C terminus of BC protein VgrG is essential to T6SS function in *A. baumannii* (20). Considering that structural information on T6SS components from this pathogen is sparse—Hcp is the only known structure so far described (21)—and given the important differences between the T6SS of *A. baumannii* and that of *E. coli*, we sought to structurally characterize the MC protein TssL of *A. baumannii* strain ATCC 17978 (Ab17978). In this work, we report the X-ray crystal structure of the cytoplasmic domain of TssL from Ab17978 at a 2.6-Å resolution. Molecular dynamics and T6SS activity assays revealed the importance of conserved residues Asp98 and Glu99 in TssL stability and functionality. Importantly, a comparison between the structure of TssL of Ab17978 and that of other organisms identified additional unique features of the T6SS of *A. baumannii*.

RESULTS

Crystal packing. The cytoplasmic TssL region (residues 32 to 196, which we refer to as Ab-TssL-C) protein crystals belonged to the P2₁ space group diffracting up to 2.6-Å resolution and having six molecules in the asymmetric unit. The protein interfaces between chains in the crystal do not suggest any specific interactions that could result in the formation of stable quaternary structures, according to PISA Web server analysis. However, analytical ultracentrifugation experiments clearly showed equilibrium between monomeric and dimeric states in solution with c(5) peaks at sedimentation coefficients of 1.2 and 1.9, respectively. This equilibrium was displaced to the dimeric form when the protein concentration is increased from 0.5 mg/ml to 1 mg/ml, changing

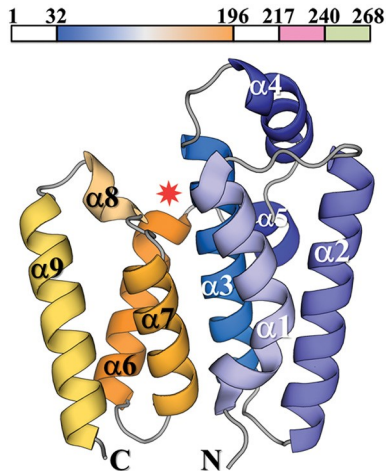


FIG 1 Schematic representation of TssL, with transmembrane helix in pink and the C-terminal periplasmic region in green. The fragment used for structural studies is shown in blue-orange, while predicted disordered regions are shown in white. The overall structure of Ab-TssL-C shows that the 9 alpha-helices are arranged in two bundle domains (blue and orange for the N and C termini, respectively) linked by a short loop between helices 5 and 6. The star marks the position of the cavity between bundles.

the c(S) peak height ratio between monomer and dimer from 0.35/0.49 to 0.41/1.33 (see Fig. S1 in the supplemental material).

Structure overview. Polypeptide chains could be traced for residues Ile33 to Lys191 in all monomers without any gap in the electron density map. The average root mean square deviation (RMSD) value between the multiple copies within the asymmetric unit was 0.225 Å, showing that all of them had nearly identical configurations.

Ab-TssL-C displays an alpha-helical bundle topology consisting of a couple of antiparallel helical bundles connected by a short loop (Fig. 1). Alpha-helices 1 to 5 form the N-terminal domain. Among them, helix α_2 , with a length of approximately 30 Å, is the longest helix in the structure. The first turn of helix α_1 is bent almost 45°, in the region where it interacts strongly with helix α_2 , while helix α_4 is tilted on top of helices α_2 and α_5 protruding from this bundle. The smaller C-terminal domain is formed by alpha-helices 6, 7, and 9 and a short 3_{10} helix (α_8). These two domains interact through interdomain side chain contacts, forming a large surface composed almost entirely of hydrophobic residues from helices α_1 , α_3 , and α_7 . Ab-TssL-C is a compact structure with a volume of 28,030 Å³ showing no intermolecular channels, but with one cavity on top of the domain interface with a volume of 350 Å³. Residues Ala95, Asp98, Glu99, Ile101, Val102, Glu113, Trp116, Leu117, Pro120, Glu122, Leu123, Ser128, Glu129, Ala131, Gly132, Phe164, and Gly166 surround this cavity. Residues Asp98 and Glu99 play a central role in this region, connecting, through H bonds, helix α_3 with residues from both helix-bundle domains. The Asp98 carboxyl group interacts with Trp116 from helix α_2 and the N main chain atoms of Leu121 and Gln122, at helix α_5 . The Glu99 carboxyl group interacts with Arg169 and the main chain of Gly166, two residues placed at helix α_8 (Fig. 2).

The electrostatic potential surface of TssL shows a balanced distribution of charge density, with a small area of negatively charged residues in the smaller C-terminal bundle and a positively charged area in the N-terminal bundle, suggesting a putative region for the interaction with the phosphate groups of the inner membrane lipids. The walls of the aforementioned cavity present a neutral charge, with predominantly hydrophobic residues, and a negative region at the top of the N-terminal bundle and a positive region in the opposite wall. The presence of two acidic residues Asp98 and Glu99 in this patch, strictly conserved among the TssL proteins in bacteria, confers a distinctive negatively charged area at the bottom of the cavity, where the two domains are close to each other (Fig. 3). The level of conservation for each residue among bacterial species was mapped in the Ab-TssL-C structure. Residues in the external

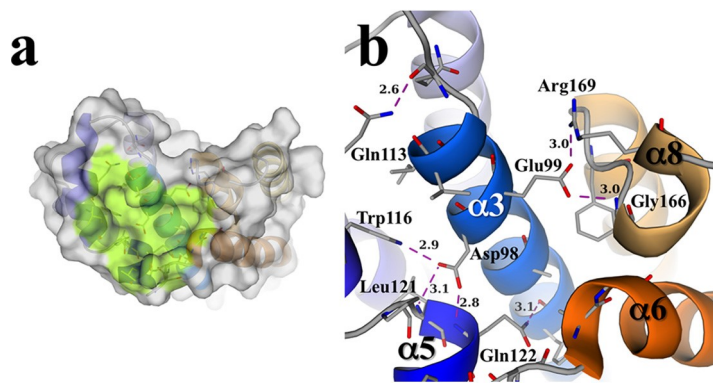


FIG 2 (a) Protein surface around the cavity (green) found in the interface between both bundle domains of Ab-TssL-C. (b) H-bond interactions between residues forming the cavity; note the central position of residues Asp98 and Glu99. All distances are in angstroms.

surface of the N-terminal domain are poorly conserved, while residues in the solvent-exposed surface of the C-terminal domain exhibit a moderate degree of conservation. Of note, we observed a high degree of conservation among residues at the interface between both domains, suggesting that these residues may be critical for protein stability and/or function. In addition, residues surrounding the cavity, particularly Asp98 and Glu99, are highly conserved (Fig. 3). To determine the effect of altering these residues on Ab-TssL-C structure and function, we performed mutational studies *in silico* and *in vivo*.

***In silico* studies.** To better understand the role of Asp98 and Glu99 in the Ab-TssL-C structure, we studied the behavior of Asp98Ala and Glu99Ala mutations using molecular dynamics. The RMSD per residue in the wild type (WT), the Asp98Ala and Glu99Ala mutants, and the double mutant variant during 500-ns dynamics is shown in Fig. 4. WT Ab-TssL-C shows the uppermost stability among the studied systems, with the highest frequency of conformers occurring at low RMSD. The Asp98Ala mutant dynamics reveal the presence of two conformers, with the most probable conformer having an RMSD value close to 0.3 nm. A different behavior was observed for the Glu99Ala mutant and the double mutant. Both variants had greater amplitude in their RMSDs, having maximum values above 0.4 nm.

Root mean square fluctuation (RMSF) analyses showed that the largest fluctuations for the Asp98Ala mutant are in the region of the cavity, while the Glu99Ala mutation primarily affects the $\alpha 8$ helix region (around residue 170). The double mutant showed

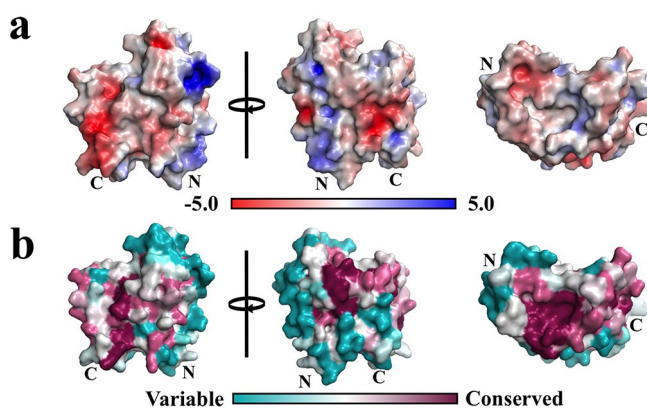


FIG 3 (a) Electrostatic surface of Ab-TssL-C, showing the distribution of positively and negatively charged regions. The top view shows the cavity region on the right side panels. (b) Conservation scores of Ab-TssL-C surface residues, showing a higher degree of conservation in the region between bundles and around the cavity. N- and C-terminal bundles are labeled for clarity.

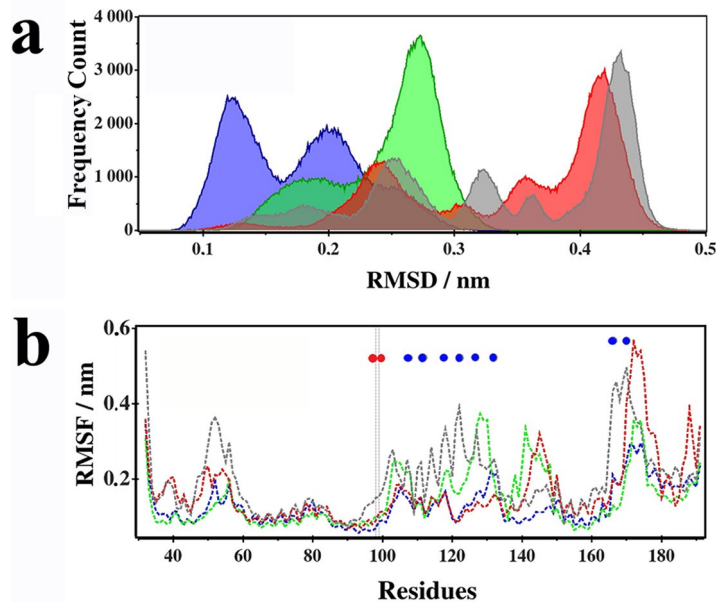


FIG 4 (a) Overall RMSD values, from 500 ns of molecular dynamics. WT Ab-TssL-C exhibits transition between two states, while different mutations affect the behavior of the protein with different results. (b) RMSF values, per residue, from 500 ns of molecular dynamics. Residues forming the cleft are labeled with blue dots, and mutated residues are labeled with red ones. In both panels, WT TssL is shown in blue, the Asp98Ala mutant is in green, the Glu99Ala mutant is in red, and the Asp98Ala-Glu99Ala double mutant is in gray.

differences from the WT in both regions. Interestingly, the double mutation reduced the RMSD values observed for both point mutation systems in the region connecting alpha-helices 6 and 7 (around residue 140) (Fig. 4). The number of intraprotein hydrogen bonds (HB) was 0.565 nm around each mutation, thus covering up to two hydration shells. The most probable HB number around residue 98 is 4 in the Asp98Ala mutant and 6 in WT TssL. In contrast, the Glu99Ala mutation does not alter the most probable HB number (i.e., 5) around residue 99. In each case, the double mutant behaved similarly to the single mutant (Fig. S2). The solvent-accessible surface area (SASA) around residues 98 and 99 also showed a different response to mutations. While for the Asp98Ala mutation the SASA value of this residue increased compared with that of the WT ($0.23 \pm 0.08 \text{ nm}^2$ and 0.17 ± 0.06 , respectively), in the Glu99Ala mutant, the SASA of residue 99 was reduced ($0.36 \pm 0.17 \text{ nm}^2$ for the WT and $0.25 \pm 0.11 \text{ nm}^2$ for the mutant). In both cases, the double mutation reduced the SASA of the analyzed residue to $0.12 \pm 0.08 \text{ nm}^2$ around residue 98 and $0.1 \pm 0.1 \text{ nm}^2$ around residue 99. The SASA value for the whole protein is $98 \pm 3 \text{ nm}^2$ for the WT protein, slightly larger for the Asp98Ala mutant ($99 \pm 2 \text{ nm}^2$) and remarkably smaller for the Glu99Ala mutant ($94 \pm 3 \text{ nm}^2$) and the double mutant ($93 \pm 3 \text{ nm}^2$) (Fig. S2).

In vivo functional assays. In light of the observed structural changes caused by the mutation of conserved residues Asp98 and Glu99 to alanine, we tested whether these mutations affected TssL function in *A. baumannii*. To this end, we performed functional Hcp secretion assays on *tssL* mutant strains of *A. baumannii* ATCC 17978 (Ab17978 $\Delta tssL$) expressing plasmid-borne 6 \times His-tagged TssL variants. As mentioned earlier, Hcp secretion is a hallmark of T6SS activity; thus, if expression of a particular TssL variant restores Hcp secretion in Ab17978 $\Delta tssL$, it indicates that the TssL variant is a functional protein. As expected, we detected Hcp in the culture supernatant of WT Ab17978 but not Ab17978 $\Delta tssL$ (Fig. 5a), indicating that WT Ab17978 has a functional T6SS while Ab17978 $\Delta tssL$ does not. Interestingly, expression of TssL Glu99Ala restored Hcp secretion in Ab17978 $\Delta tssL$ to levels comparable to those of the complemented strain expressing WT TssL. In contrast, expression of TssL Asp98Ala or the double mutant did not result in detectable levels of Hcp secretion (Fig. 5a). However, both TssL Asp98Ala

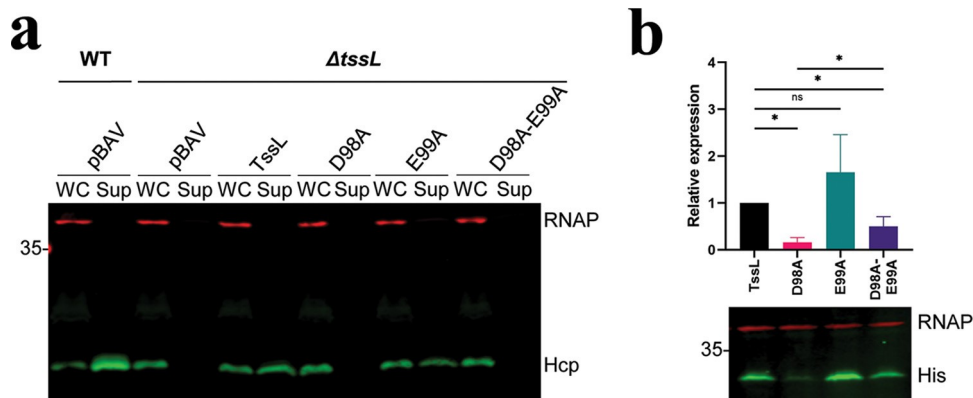


FIG 5 TssL Glu99Ala is a functional protein, while TssL variants with mutation Asp98Ala are poorly expressed. (a) Western blot of whole-cell (WC) and supernatant (Sup) fractions of Ab17978 $\Delta tssL$ expressing the indicated TssL variants or empty vector pBAV. Wild-type Ab17978 is shown as a positive control for Hcp secretion. RNA polymerase (RNAP) is included as a lysis and loading control. The Western blot is representative of five independent experiments. (b) (Top) Cumulative data from five independent experiments (means \pm standard deviations) showing the relative expression of the indicated TssL variants in Ab17978 $\Delta tssL$. Statistical analyses were performed using a Mann-Whitney test. *, $P < 0.01$. ns, not significant. (Bottom) A representative Western blot probed for the indicated 6 \times His-tagged TssL variants and RNAP (loading control) in WC fractions of Ab17978 $\Delta tssL$.

and the double mutant were expressed to significantly lower levels than WT TssL (Fig. 5b), indicating that these mutations likely impact protein stability. Notably, the double mutant was detected at significantly higher levels than the Asp98Ala mutant, suggesting that this protein is more stable than the Asp98Ala variant (Fig. 5b). Thus, the levels of protein expression *in vivo* are consistent with the results obtained from the hydrogen bond and SASA analyses. Together, our results demonstrate that TssL Glu99Ala is a functional protein and suggest that the Asp98Ala mutation results in protein instability, which is reduced when Glu99 is also mutated to alanine.

DISCUSSION

The T6SS has a key function in *Acinetobacter* species, being involved in bacterial competition and horizontal gene transfer (19). The overall architecture of the T6SS of *A. baumannii* is not known, but as in other Gram-negative bacteria, it seems to be composed of three complexes, one of them attached to the cell membrane. It is in this membrane-associated complex where TssL plays its purely structural role, with its N-terminal domain facing the cytoplasm and interacting with other members of the machinery. Despite the low sequence identity of Ab-TssL-C with known TssL structures from enteroaggregative *E. coli* (PDB code 3U66; 23.27% identity) (6), *F. novicida* (PDB code 4ACK; 18.79% identity) (7), and *V. cholerae* (PDB code 4V3I; 19.08% identity) (8), the overall folding is conserved (Fig. 6). The Ab-TssL-C structure superposes with these homologs with an RMSD value between C α atoms of 2.36, 1.12, and 4.10 Å, respectively. Interestingly, the main differences were found in the intramolecular interaction regions. The helix $\alpha 1$ was bent 45°, with a geometry similar to that observed in the *E. coli* and *V. cholerae* TssL structures, where the presence of a proline residue induces the kink. A straight geometry was observed for this helix in *F. novicida*, having an aspartic acid residue in the proline position. Despite the aspartic acid in this position, helix $\alpha 1$ is bent in Ab-TssL-C. This particular geometry is observed in all of the six chains present in the asymmetric unit, suggesting that this conformation must be a characteristic of this helix and not due to crystallographic contacts. This specific conformation might have functional significance since this N-terminal helix has been implicated in dimer formation of *E. coli* TssL. In this organism, a zipper-like model was proposed in which transmembrane helices interact as a first step, increasing the local protein concentration and then aiding the dimerization of TssL cytoplasmic domains through helix $\alpha 1$ (6). In support of this model, we observed a shift to the dimeric state in Ab-TssL-C when the protein concentration was increased.

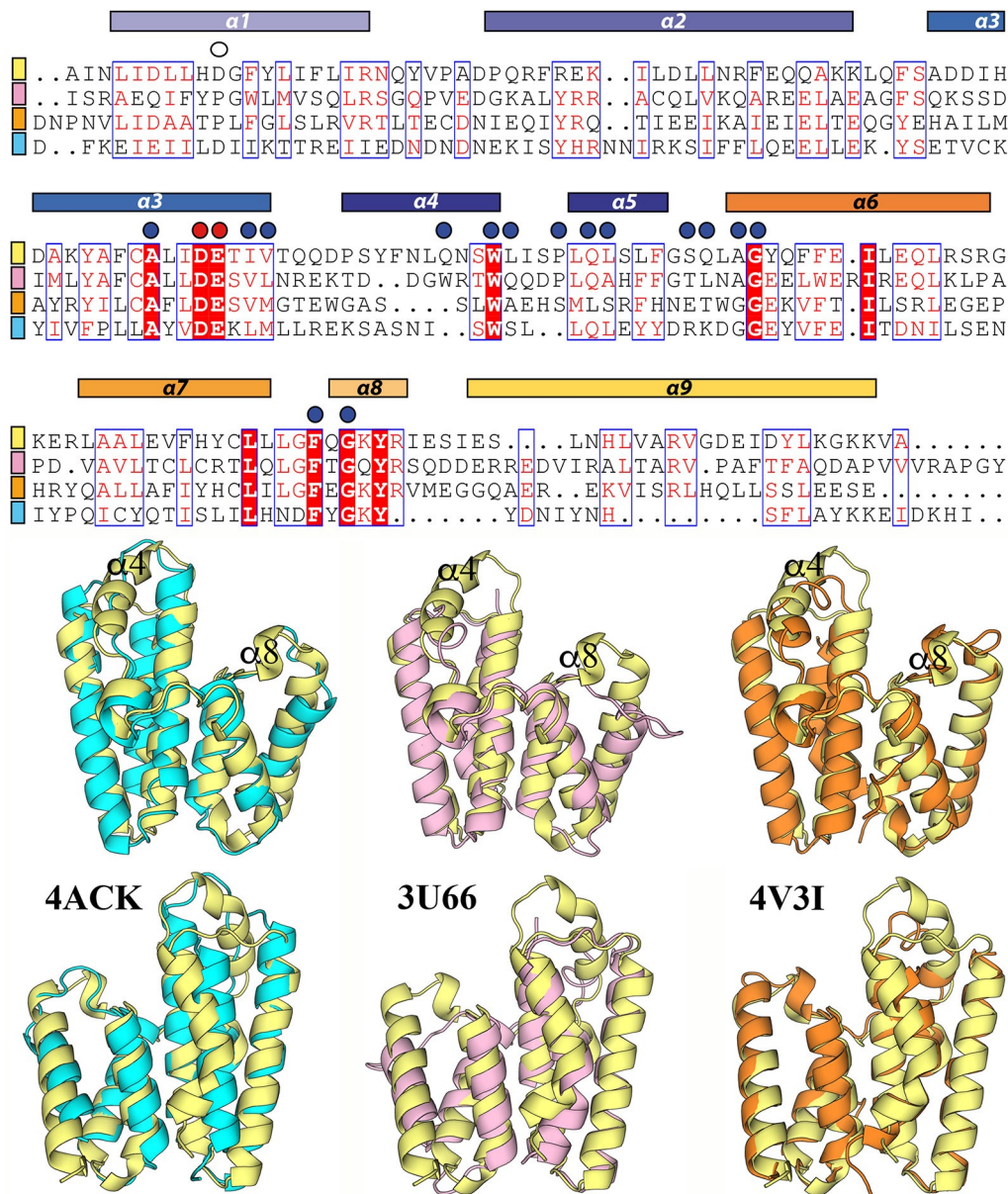


FIG 6 Sequence and structural alignments between Ab-TssL-C (yellow) and the TssL structures from *F. novicida* (PDB code 4ACK [cyan]), *E. coli* (PDB code 3U66 [pink]), and *V. cholerae* (PDB code 4V3I [orange]). Those residues belonging to the cleft are indicated with filled circles, in red positions 98 and 99; the empty circle indicates the position where helix $\alpha 1$ is bent. In the second panel helices $\alpha 4$ and $\alpha 8$, the major structural difference between structures, are labeled.

A second major difference is seen in helix $\alpha 4$, which is longer and protrudes more so than the equivalent ones (if any) from the surface of the N-terminal bundle. This region has been proposed to be a key site for binding TssK, a component of the cytoplasmic BC. Finally, another important difference with the homologous structures is the presence of a short 3_{10} helix (helix $\alpha 8$) and the length of helix $\alpha 9$, two characteristics shared with the *V. cholerae* TssL. In *E. coli* and *F. novicida*, residues in this region form a loop, indicating a high degree of flexibility. This loop has been shown to be responsible for the interaction with TssE, a second component of the BC. The variability in sequence and structure in these last two regions might be crucial for the specificity of TssL for the BC components TssK and TssE, as suggested by Zoued et al. (3). The conserved cleft between bundles has been shown to be required for the interaction with the cytoplasmic domain of TssM (3). Remarkably, among the 10

residues strictly conserved between the known TssL structures, 7 form part of the cleft. Mutation of two of them, Asp98 and Glu99 (numbering of Ab-TssL-C), disrupt the interaction with TssM and the functionality of the T6SS without affecting the stability of TssL in *V. cholerae* (3) and *F. tularensis* (22).

To analyze the impact of mutations to the strictly conserved residues Asp98 and Glu99 on the structure and functionality of *A. baumannii* TssL, we performed molecular dynamics analyses complemented with *in vivo* experiments. For molecular dynamics, we did not consider TssL regions that are not covered in the crystal structure, e.g., the TMH. Despite the fact that we could not affirm that the effect of these residues is negligible in the dynamics of the full-length protein, we considered that this effect would be equivalent between WT and mutant variants of Ab-TssL-C. The RMSD values calculated from 500-ns simulations show the WT Ab-TssL-C protein fluctuating between two similar conformations with little difference between them, and the same behavior was observed in the Asp98Ala mutant. However, one of the conformations had a higher probability in this system, exhibiting a larger RMSD value than any of the two WT conformers. Great fluctuations between different conformers were observed in the Glu99Ala and the double mutant systems. In both cases, the most probable conformation is the one with the larger RMSD value. These last two systems show the minimal total SASA among the studied ones, suggesting that the most probable conformation is more compact than those of WT Ab-TssL-C and the Asp98Ala mutant. When the local environment of mutated residues was analyzed, the modification of residue 99 was not found to alter the hydrogen-bonding network, reducing the SASA of this residue without affecting movements of residues in the cavity region. These minimal structural changes are consistent with our results showing that the Glu99Ala mutant is a functional protein. In contrast, the mutation of residue 98 drastically reduces the number of hydrogen bonds, increasing the SASA of this residue and RMSF values in the whole cavity. These results suggest that TssL is destabilized by the Asp98Ala mutation, consistent with the low levels of protein detected for this variant in our *in vivo* studies. The molecular dynamics results also suggest that the double mutation could compensate the effect of the Asp98Ala mutation, compacting the protein structure in the cavity region by increasing hydrophobic interactions. Indeed, the double mutant was expressed more strongly than the Asp98Ala variant. Moreover, although the predicted changes in the geometry around the cleft resulting from the Asp98Ala mutation would likely hamper the interaction between TssL and TssM in *A. baumannii*, as has been reported in *V. cholerae* (3) and *F. tularensis* (22), the expression of variants containing this mutation (i.e., Asp98Ala and Asp98Ala-Glu99Ala) was lower than that of WT TssL. Thus, we cannot make conclusions regarding the functionality of these two variants. Collectively, our work shows that unlike in other organisms, a Glu99Ala mutant of TssL retains functionality in *A. baumannii*. Future work will further characterize the role of Asp98 in *A. baumannii* TssL stability and interaction with TssM and other components of the T6SS machinery.

The T6SS presents interesting particularities in *A. baumannii*; however, little is known about the architecture of this secretion system in this pathogen. Considering that structural information on T6SS components from this Gram-negative bacillus is exiguous, the crystal structure and *in silico* and *in vivo* studies of TssL presented here represent an important improvement in our understanding of the T6SS of *A. baumannii*.

MATERIALS AND METHODS

Cloning, expression, and purification. TssL from *A. baumannii* (ATCC 17978; A15_1310) is a 268-residue protein with a predicted transmembrane helix from residues 217 to 240 and 28 residues forming the C-terminal periplasmic region. A gene fragment encoding the cytoplasmic TssL residues 32 to 196 (Ab-TssL-C) was amplified by standard PCR from genomic DNA. Residues 1 to 31 and 197 to 216 were excluded for crystallization purposes since they are predicted to constitute disordered regions. The sense primer 5'-ACAG**CTAGCG**CAATTAATCTGATTGATTTA, containing an internal NheI restriction site (bold), and the antisense primer 5'-ACACT**CGAG**TTATGCCACTTTTTCCCTTT, introducing an XhoI restriction site (bold) with a stop codon (underlined), were used for amplification. The PCR product was digested with NheI and XhoI (New England BioLabs [NEB], Ipswich, MA) and cloned into the pET28-a (Merck Novagen, Darmstadt, Germany) expression vector. The recombinant plasmid was transformed

TABLE 1 Data collection and refinement statistics^a

Parameter	Value(s)
Wavelength (Å)	1.073
Resolution range (Å)	48.48–2.59 (2.68–2.59)
Space group	P 1 21 1
Unit cell: a, b, c (Å)	96.8, 78.8, 96.9
α, β, γ (°)	90, 119.8, 90
Total reflections	109,140 (11,645)
Unique reflections	37,828 (4,386)
Multiplicity	2.9 (2.7)
Completeness (%)	95.8 (90.6)
Mean $I/\sigma(I)$	6.88 (1.88)
Wilson B factor (Å ²)	31.43
R-merge	0.08 (0.37)
R-meas	0.11 (0.52)
CC1/2	0.99 (0.88)
CC*	0.99 (0.96)
Reflections used in refinement	37,700 (3,555)
Reflections used for R-free	1,803 (175)
R-work	0.20 (0.27)
R-free	0.26 (0.41)
CC (work)	0.95 (0.85)
CC (free)	0.91 (0.60)
No. of nonhydrogen atoms	8,196
Protein atoms	7,948
Protein residues	960
RMS (bonds) (Å)	0.010
RMS (angles) (°)	1.25
Ramachandran favored (%)	99
Ramachandran allowed (%)	1.3
Ramachandran outliers (%)	0
Rotamer outliers (%)	0.59
Clashscore	7.51
Avg B factor (Å ²)	39.39
Protein	39.76
Solvent	27.53
No. of TLS groups	6

^aStatistics for the highest-resolution shell are shown in parentheses. CC, correlation coefficient; CC1/2, CC between intensities of crystallographic random half data sets; CC*, estimation of the CC of the full data set against the true intensities; TLS, translation/libration/screw.

into competent *E. coli* DH5 α cells (Merck Novagen) for DNA production and purification, with the integrity of the construct verified by sequencing. Finally, the plasmid was transformed into BL21 RIL (DE3) CodonPlus cells (Merck Novagen) for protein production. Cells were grown at 310 K in 0.5 liter of 2 \times yeast extract-tryptone (YT) kanamycin-supplemented medium until an optical density at 600 nm (OD₆₀₀) of 0.8 was reached. At this point, isopropyl- β -D-1-thiogalactopyranoside (IPTG) was added to a final concentration of 1 mM and the culture was grown for an additional 4 h at 303 K. The bacterial cells were harvested by centrifugation (20,000 $\times g$, 15 min, 277 K) and resuspended in lysis buffer (350 mM NaCl, 20 mM Tris [pH 8.0], 1 mM β -mercaptoethanol [β ME], and 10 mM imidazole). After sonication, the lysate was cleared by ultracentrifugation at 140,000 $\times g$ for 30 min at 277 K. The soluble fraction was loaded into a HisTrap column (GE Healthcare, Freiburg, Germany) equilibrated with lysis buffer. The protein was subsequently eluted from the column using an imidazole gradient, from 10 to 500 mM. Fractions containing TssL were concentrated using Amicon Ultra 10,000-molecular-weight-cutoff (MWCO) centrifugal filter units (Merck Millipore, Darmstadt, Germany) and further purified by gel filtration using a Superdex75 16/60 column (GE Healthcare, Freiburg, Germany) equilibrated with 150 mM NaCl, 20 mM Tris-HCl (pH 8.0), and 1 mM dithiothreitol (DTT). The protein eluted in a single peak and the pooled peak fractions were concentrated, as previously described, to 15 mg ml⁻¹ for crystallization trials. All purification steps were carried out at room temperature. The purified product was analyzed by SDS-PAGE.

Crystallization and data collection and processing. Crystallization experiments were carried out at 295 K using the vapor diffusion method (sitting drop). Crystals were obtained by mixing 1 μ l of purified protein with 1 μ l of reservoir solution: 10% polyethylene glycol 6000 (PEG 6000) and 10 mM MgCl₂. Crystals were cryoprotected with this condition supplemented with 30% (vol/vol) glycerol, mounted in nylon loops, and flash-cooled by immersion in liquid nitrogen. Diffraction data were collected at the BL13-XALOC beamline of the ALBA Synchrotron (Cerdanyola del Valles, Spain). Crystallographic data were processed using XDS (23) and Aimless (24). Details of reflection data are presented in Table 1.

Structure determination and refinement. Despite initial unsuccessful molecular replacement (MR) attempts using known structures as search models, a solution was finally found using the AutoRickshaw platform and the MoRDa automatic pipeline (25, 26), with the protein sequence as input. The Phenix

TABLE 2 Primers used in the generation of TssL mutant and pBAVMCS constructs

Primer	Sequence
TssLFWBamHI (Ab17978 into pBAV)	ATAGGATCCATGTCACAATCTACAGGTGCTCC
TssLRVPstI6His (Ab17978 into pBAV)	ATACTGCAGTCAGTGGTGATGATGGTGGTGAGGTAAGTAAATAGTAATATGTCCTGC
Mutant tssL Ab17978 F	GGATTCCAGAAACGATTTGTATTTATGTTCCGGCTGGATTCCAAGATATCAGTATTGAGCTGATTGCGGTCA TGAACGCTTAAAGATAAAGGAGAGAAAAGCGATTGTGTAGGCTGGAGCTGCTTCG
Mutant tssL Ab17978 R	CCAATGATGATATAGATTACTGGTGATCTCGACTTTTTTTTATTTCGATTGCAAACTCGAATAGAAGTTGG TTTTTCTGAGCCATTTCTTCCATCACATATGAATATCCTCCTTAGTTCCTATTCCG
TssLDEtoAA1 17978	TGCTGGGTACGATCGTTGCAGCAATTAGCGCACAAAACG
TssLDEtoAA2 17978	CGTTTTGTGCGCTAATTGTGCAACGATCGTAACCCAGCA
TssLD98toA1 17978	TGGGTTACGATCGTTTCAGCAATTAGCGCACAAAACG
TssLD98toA2 17978	CGTTTTGTGCGCTAATTGTGCAACGATCGTAACCCCA
TssLE99toA1 17978	GCTGGGTTACGATCGTTGCATCAATTAGCGCACAA
TssLE99toA2 17978	TTGTGCGCTAATTGATGCAACGATCGTAACCCAGC

suite (27) was used for structural refinement and Coot (28) for manual building and addition of water molecules. Statistical details of the final model are given in Table 1. Analysis of the protein-protein interactions and amino acid conservation were performed using the PISA (29) and ConSurf Web servers (30), respectively. The surface of the protein was analyzed using CASTp (31). Molecular images were generated using PyMOL (32) or Chimera (33).

Analytical ultracentrifugation. Proteins samples were diluted to final concentrations of 0.5 and 1 mg ml⁻¹ and precleared at 16,000 × *g*. Sedimentation velocity experiments were run at 293 K in an Optima KL-I analytical ultracentrifuge (Beckman Coulter, USA) with an An50-Ti rotor and standard double-sector Epon charcoal center pieces (1.2-cm optical path length). Measurements were performed at 48,000 rpm, registering successive entries every minute at 280 nm. Rayleigh interferometric detection was used to monitor the evolution of the concentration gradient in function of time and radial position, and the data were analyzed using SedFit software (version 14.7) (34).

Molecular dynamics studies. Mutant variants of Ab-TssL-C were generated in Coot (28), modifying residues Asp98 and/or Glu99 from the crystallographic structure. Simulation boxes included one protein molecule (WT or mutant), 13,590 water molecules (SPC/E model [35]), and Na⁺ ions for a zero net charge. Initial equilibration was carried out for each system using the steepest descent method until the potential energy gradient was lower than 1,000 kJ mol⁻¹. Protein backbone movements were restrained using a harmonic potential with a force constant of 1,000 kJ mol⁻¹ nm⁻². In a second equilibration step, the system was attached to a constant number of particles, volume, and temperature (NVT) ensemble for 500 ps, maintaining the backbone restrictions and assigning random speeds through a Maxwell-Boltzmann distribution at 300.15 K. During the last equilibration step, the system was subjected to a constant number of particles, pressure, and temperature (NPT) ensemble for 500 ps, keeping the backbone restrictions and maintaining a constant pressure of 1 bar. For the production phase, the restrictions were removed and each system was analyzed for 500-ns runs using the GROMACS package (36) and the GROMOS 54A7 force field (37).

During equilibration and production processes, protein and nonprotein groups (water and ions) were independently coupled using the velocity-rescale thermostat and the Berendsen barostat. Electrostatic interactions were calculated applying the reaction field method (38) with a cutoff for van der Waals and Coulomb interactions of 1.0 nm. LINCS algorithm was applied to constrain solute bonds (39). A time step of 2 fs was used throughout the simulations.

Generation of tssL mutant and pBAVMCS constructs. Primers used in this study are listed in Table 2. The genetic manipulation and *in vivo* experiments were performed with *A. baumannii* ATCC 17978 (Ab17978) lacking its large conjugative plasmid pAB3. Marked mutant strains were generated by recombineering, as described previously (40). Selection for marked mutants was carried out using kanamycin (12.5 μg/ml). Selection for clean mutants was performed using carbenicillin (400 μg/ml). Clean mutants were subsequently passaged on LB until they were no longer carbenicillin resistant. Mutant strains were verified by PCR and sequencing.

Construct pBAV-TssL-6×His was generated by restriction cloning using the BamHI and PstI sites of pBAVMCS (41). This plasmid was then used as a template to make point mutants of TssL using the QuikChange II site-directed mutagenesis kit (Agilent Technologies, Santa Clara, CA) according to the manufacturer's instructions. Selection was carried out using kanamycin (30 μg/ml). All constructs were verified by PCR and sequencing.

Hcp secretion assay and Western blotting. The Hcp secretion assay was performed as described previously, with few modifications (20). Overnight cultures of wild-type Ab17978 or Ab17978 Δ*tssL* expressing variants of TssL or a vector control were diluted into fresh LB plus kanamycin (30 μg/ml) to an OD₆₀₀ of 0.05 and grown at 30°C with shaking until they reached an OD₆₀₀ of 0.4 to 0.7. Cells were then pelleted by centrifugation. Cells were resuspended in Laemmli buffer to a final OD of 0.01, while the supernatant fraction was centrifuged once again to pellet residual cells. Supernatant proteins were subsequently precipitated with trichloroacetic acid, as previously described (16), and resuspended in Laemmli buffer. OD-normalized volumes of whole cells or supernatants were loaded onto 15% SDS-PAGE gels for separation, transferred to a nitrocellulose membrane, and probed with polyclonal rabbit anti-Hcp (1:1,000 [41]), polyclonal rabbit anti-6×His (1:2,000; Invitrogen, Waltham, MA), or monoclonal mouse anti-RNA polymerase (1:2,600; Biologend, San Diego, CA), where appropriate. Western blots were then

probed with IRDye-conjugated anti-mouse and anti-rabbit secondary antibodies (both at 1:15,000; LI-COR Biosciences, Lincoln, NE) and visualized with an Odyssey CLx imaging system (LI-COR Biosciences).

The relative expression of TssL variants was determined using Image Studio 5.2 (https://www.licor.com/bio/help/imagestudio5/index.html#Introduction_help.html%3FTocPath%3D_____2). The overall TssL variant expression was defined as the band intensity of the His signal divided by the band intensity of the RNA polymerase (RNAP) signal. Given that the RNAP signal is used as a loading control, a higher His/RNAP value indicates a higher level of protein expression. The data are presented as relative expression, where the His/RNAP value of WT TssL is defined as 1.

Accession number(s). Coordinates and structure factors have been deposited in the Protein Data Bank under PDB code 6Y4R.

SUPPLEMENTAL MATERIAL

Supplemental material is available online only.

SUPPLEMENTAL FILE 1, PDF file, 0.2 MB.

ACKNOWLEDGMENTS

F.M.R., E.S., and A.R. thank the staff at the BL13-XALOC beamline of the ALBA Synchrotron (Cerdanyola del Valles, Spain) and the staff at the Molecular Interactions Facility of the CIB. C.G.F. and Y.R.E. thank J. R. Grigera for his teachings.

This work was supported by grants from Universidad Nacional Arturo Jauretche and Consejo Nacional de Investigaciones Científicas y Técnicas (CONICET), by National Institutes of Health grant 1R01AI125363 to M.F.F., and by grant BFU2016-77835-R of the Spanish Ministry of Economy and Competitiveness to A.R. J.L. is funded by the Washington University Chancellor's Graduate Fellowship.

The funders had no role in this study.

REFERENCES

1. Nguyen VS, Douzi B, Durand E, Roussel A, Cascales E, Cambillau C. 2018. Towards a complete structural deciphering of type VI secretion system. *Curr Opin Struct Biol* 49:77–84. <https://doi.org/10.1016/j.sbi.2018.01.007>.
2. Leiman PG, Basler M, Ramagopal UA, Bonanno JB, Sauder JM, Pukatzki S, Burley SK, Almo SC, Mekalanos JJ. 2009. Type VI secretion apparatus and phage tail-associated protein complexes share a common evolutionary origin. *Proc Natl Acad Sci U S A* 106:4154–4159. <https://doi.org/10.1073/pnas.0813360106>.
3. Zoued A, Cassaro CJ, Durand E, Douzi B, Espana AP, Cambillau C, Journet L, Cascales E. 2016. Structure-function analysis of the TssL cytoplasmic domain reveals a new interaction between the type VI secretion base-plate and membrane complexes. *J Mol Biol* 428:4413–4423. <https://doi.org/10.1016/j.jmb.2016.08.030>.
4. Rapisarda C, Cherrak Y, Kooger R, Schmidt V, Pellarin R, Logger L, Cascales E, Pilhofer M, Durand E, Fronzes R. 2019. In situ and high-resolution cryo-EM structure of a bacterial type VI secretion system membrane complex. *EMBO J* 38:e100886. <https://doi.org/10.15252/embj.2018100886>.
5. Durand E, Nguyen VS, Zoued A, Logger L, Pehau-Arnaudet G, Aschtgen MS, Spinelli S, Desmyter A, Bardiaux B, Dujeancourt A, Roussel A, Cambillau C, Cascales E, Fronzes R. 2015. Biogenesis and structure of a type VI secretion membrane core complex. *Nature* 523:555–560. <https://doi.org/10.1038/nature14667>.
6. Durand E, Zoued A, Spinelli S, Watson PJ, Aschtgen MS, Journet L, Cambillau C, Cascales E. 2012. Structural characterization and oligomerization of the TssL protein, a component shared by bacterial type VI and type IVb secretion systems. *J Biol Chem* 287:14157–14168. <https://doi.org/10.1074/jbc.M111.338731>.
7. Robb CS, Nano FE, Boraston AB. 2012. The structure of the conserved type six secretion protein TssL (DotU) from *Francisella novicida*. *J Mol Biol* 419:277–283. <https://doi.org/10.1016/j.jmb.2012.04.003>.
8. Chang JH, Kim YG. 2015. Crystal structure of the bacterial type VI secretion system component TssL from *Vibrio cholerae*. *J Microbiol* 53:32–37. <https://doi.org/10.1007/s12275-015-4539-0>.
9. Aschtgen MS, Zoued A, Lloubes R, Journet L, Cascales E. 2012. The C-tail anchored TssL subunit, an essential protein of the enteroaggregative *Escherichia coli* Sci-1 type VI secretion system, is inserted by YidC. *Microbiologyopen* 1:71–82. <https://doi.org/10.1002/mbo3.9>.
10. Zoued A, Duneau JP, Durand E, Espana AP, Journet L, Guerlesquin F, Cascales E. 2018. Tryptophan-mediated dimerization of the TssL trans-membrane anchor is required for type VI secretion system activity. *J Mol Biol* 430:987–1003. <https://doi.org/10.1016/j.jmb.2018.02.008>.
11. Wong D, Nielsen TB, Bonomo RA, Pantapalangkoor P, Luna B, Spellberg B. 2017. Clinical and pathophysiological overview of *Acinetobacter* infections: a century of challenges. *Clin Microbiol Rev* 30:409–447. <https://doi.org/10.1128/CMR.00058-16>.
12. Howard A, O'Donoghue M, Feeny A, Sleator RD. 2012. *Acinetobacter baumannii*: an emerging opportunistic pathogen. *Virulence* 3:243–250. <https://doi.org/10.4161/viru.19700>.
13. Mulani MS, Kamble EE, Kumkar SN, Tawre MS, Pardesi KR. 2019. Emerging strategies to combat ESKAPE pathogens in the era of antimicrobial resistance: a review. *Front Microbiol* 10:539. <https://doi.org/10.3389/fmicb.2019.00539>.
14. Shlaes DM, Bradford PA. 2018. Antibiotics—from there to where? How the antibiotic miracle is threatened by resistance and a broken market and what we can do about it. *Pathog Immun* 3:19–43. <https://doi.org/10.20411/pai.v3i1.231>.
15. Henry R, Vithanage N, Harrison P, Seemann T, Coutts S, Moffatt JH, Nation RL, Li J, Harper M, Adler B, Boyce JD. 2012. Colistin-resistant, lipopolysaccharide-deficient *Acinetobacter baumannii* responds to lipopolysaccharide loss through increased expression of genes involved in the synthesis and transport of lipoproteins, phospholipids, and poly-beta-1,6-N-acetylglucosamine. *Antimicrob Agents Chemother* 56:59–69. <https://doi.org/10.1128/AAC.05191-11>.
16. Weber BS, Miyata ST, Iwashkiw JA, Mortensen BL, Skaar EP, Pukatzki S, Feldman MF. 2013. Genomic and functional analysis of the type VI secretion system in *Acinetobacter*. *PLoS One* 8:e55142. <https://doi.org/10.1371/journal.pone.0055142>.
17. Repizo GD, Espariz M, Seravalle JL, Salcedo SP. 2019. Bioinformatic analysis of the type VI secretion system and its potential toxins in the *Acinetobacter* genus. *Front Microbiol* 10:2519. <https://doi.org/10.3389/fmicb.2019.02519>.
18. Lewis JM, Deveson Lucas D, Harper M, Boyce JD. 2019. Systematic identification and analysis of *Acinetobacter baumannii* type VI secretion system effector and immunity components. *Front Microbiol* 10:2440. <https://doi.org/10.3389/fmicb.2019.02440>.
19. Ringel PD, Hu D, Basler M. 2017. The role of type VI secretion system effectors in target cell lysis and subsequent horizontal gene transfer. *Cell Rep* 21:3927–3940. <https://doi.org/10.1016/j.celrep.2017.12.020>.
20. Lopez J, Ly PM, Feldman MF. 2020. The tip of the VgrG spike is essential

- to functional type VI secretion system assembly in *Acinetobacter baumannii*. mBio 11:e02761-19. <https://doi.org/10.1128/mBio.02761-19>.
21. Ruiz FM, Santillana E, Spinola-Amilibia M, Torreira E, Culebras E, Romero A. 2015. Crystal structure of Hcp from *Acinetobacter baumannii*: a component of the type VI secretion system. PLoS One 10:e0129691. <https://doi.org/10.1371/journal.pone.0129691>.
 22. Broms JE, Meyer L, Lavander M, Larsson P, Sjostedt A. 2012. DotU and VgrG, core components of type VI secretion systems, are essential for *Francisella LVS* pathogenicity. PLoS One 7:e34639. <https://doi.org/10.1371/journal.pone.0034639>.
 23. Kabsch W. 2010. Xds. Acta Crystallogr D Biol Crystallogr 66:125–132. <https://doi.org/10.1107/S0907444909047337>.
 24. Winn MD, Ballard CC, Cowtan KD, Dodson EJ, Emsley P, Evans PR, Keegan RM, Krissinel EB, Leslie AG, McCoy A, McNicholas SJ, Murshudov GN, Pannu NS, Potterton EA, Powell HR, Read RJ, Vagin A, Wilson KS. 2011. Overview of the CCP4 suite and current developments. Acta Crystallogr D Biol Crystallogr 67:235–242. <https://doi.org/10.1107/S0907444910045749>.
 25. Vagin A, Lebedev A. 2015. MoRDa, an automatic molecular replacement pipeline. Acta Crystallogr A 71:s19. <https://doi.org/10.1107/S2053273115099672>.
 26. Panjikar S, Parthasarathy V, Lamzin VS, Weiss MS, Tucker PA. 2005. Auto-rickshaw: an automated crystal structure determination platform as an efficient tool for the validation of an X-ray diffraction experiment. Acta Crystallogr D Biol Crystallogr 61:449–457. <https://doi.org/10.1107/S0907444905001307>.
 27. Adams PD, Afonine PV, Bunkoczi G, Chen VB, Davis IW, Echols N, Headd JJ, Hung LW, Kapral GJ, Grosse-Kunstleve RW, McCoy AJ, Moriarty NW, Oeffner R, Read RJ, Richardson DC, Richardson JS, Terwilliger TC, Zwart PH. 2010. PHENIX: a comprehensive Python-based system for macromolecular structure solution. Acta Crystallogr D Biol Crystallogr 66:213–221. <https://doi.org/10.1107/S0907444909052925>.
 28. Emsley P, Lohkamp B, Scott WG, Cowtan K. 2010. Features and development of Coot. Acta Crystallogr D Biol Crystallogr 66:486–501. <https://doi.org/10.1107/S0907444910007493>.
 29. Krissinel E, Henrick K. 2007. Inference of macromolecular assemblies from crystalline state. J Mol Biol 372:774–797. <https://doi.org/10.1016/j.jmb.2007.05.022>.
 30. Ashkenazy H, Abadi S, Martz E, Chay O, Mayrose I, Pupko T, Ben-Tal N. 2016. ConSurf 2016: an improved methodology to estimate and visualize evolutionary conservation in macromolecules. Nucleic Acids Res 44:W344–W350. <https://doi.org/10.1093/nar/gkw408>.
 31. Tian W, Chen C, Lei X, Zhao J, Liang J. 2018. CASTp 3.0: computed atlas of surface topography of proteins. Nucleic Acids Res 46:W363–W367. <https://doi.org/10.1093/nar/gky473>.
 32. DeLano W. 2002. The PyMOL molecular graphics system. DeLano Scientifics, Palo Alto, CA.
 33. Pettersen EF, Goddard TD, Huang CC, Couch GS, Greenblatt DM, Meng EC, Ferrin TE. 2004. UCSF Chimera—a visualization system for exploratory research and analysis. J Comput Chem 25:1605–1612. <https://doi.org/10.1002/jcc.20084>.
 34. Schuck P. 2000. Size-distribution analysis of macromolecules by sedimentation velocity ultracentrifugation and lamm equation modeling. Biophys J 78:1606–1619. [https://doi.org/10.1016/S0006-3495\(00\)76713-0](https://doi.org/10.1016/S0006-3495(00)76713-0).
 35. Berendsen HG, Grigera JR, Straatsma TP. 1987. The missing term in effective pair potentials. J Phys Chem 91:6269–6271. <https://doi.org/10.1021/j100308a038>.
 36. Hess B, Kutzner C, van der Spoel D, Lindahl E. 2008. GROMACS 4: algorithms for highly efficient, load-balanced, and scalable molecular simulation. J Chem Theory Comput 4:435–447. <https://doi.org/10.1021/ct700301q>.
 37. Huang W, Lin Z, van Gunsteren WF. 2011. Validation of the GROMOS 54A7 force field with respect to beta-peptide folding. J Chem Theory Comput 7:1237–1243. <https://doi.org/10.1021/ct100747y>.
 38. Tironi I, Sperb R, Smith PE, van Gunsteren WF. 1995. A generalized reaction field method for molecular dynamics simulations. J Chem Phys 102:5451–5459. <https://doi.org/10.1063/1.469273>.
 39. Hess B, Bekker H, Berendsen HJC, Fraaije J. 1997. LINCS: a linear constraint solver for molecular simulations. J Comput Chem 18:1463–1472. [https://doi.org/10.1002/\(SICI\)1096-987X\(199709\)18:12<1463::AID-JCC4>3.0.CO;2-H](https://doi.org/10.1002/(SICI)1096-987X(199709)18:12<1463::AID-JCC4>3.0.CO;2-H).
 40. Tucker AT, Nowicki EM, Boll JM, Knauf GA, Burdis NC, Trent MS, Davies BW. 2014. Defining gene-phenotype relationships in *Acinetobacter baumannii* through one-step chromosomal gene inactivation. mBio 5:e01313-14. <https://doi.org/10.1128/mBio.01313-14>.
 41. Weber BS, Hennon SW, Wright MS, Scott NE, de Berardinis V, Foster LJ, Ayala JA, Adams MD, Feldman MF. 2016. Genetic dissection of the type VI secretion system in *Acinetobacter* and identification of a novel peptidoglycan hydrolase, TagX, required for its biogenesis. mBio 7:e01253-16. <https://doi.org/10.1128/mBio.01253-16>.